NANO LETTERS

Letter

pubs.acs.org/NanoLett

Phase Separation of Dirac Electrons in Topological Insulators at the Spatial Limit

Carolina Parra,[*,†,‡,§] Thiago Henrique Rodrigues da Cunha,[∥] Alex W. Contryman,[⊥] Desheng Kong,[§,#,○] Francisco Montero-Silva,[†] Pedro Henrique Rezende Gonçalves,[▽] Diogo Duarte Dos Reis,[▽] Paula Giraldo-Gallo,[◆] Rodrigo Segura,[□] Fernanda Olivares,[□] Francis Niestemski,[‡,§] Yi Cui,[§,#] Rogerio Magalhaes-Paniago,[▽] and Hari C. Manoharan[‡,§]

[†]Laboratorio Nanobiomateriales, Departamento de Física, Universidad Técnica Federico Santa María, Avenida España, 1680, Valparaíso, Chile

[‡]Department of Physics, Stanford University, Stanford, California 94305, United States

[§]Stanford Institute for Materials and Energy Sciences, SLAC National Accelerator Laboratory, Menlo Park, California 94025, United States

[∥]CTNanotubos, Universidade Federal de Minas Gerais, Rua Professor José Vieira de Mendonça 1.000, Engenho Nogueira, BH, Brazil

[⊥]Department of Applied Physics, Stanford University, Stanford, California 94305, United States

[#]Department of Materials Science and Engineering, Stanford University, Stanford, California 94305, United States

[○]National Laboratory of Solid State Microstructure, College of Engineering and Applied Sciences, and Collaborative Innovation Center of Advanced Microstructures, Nanjing University, Nanjing 210093, China

[▽]Departamento de Física, Universidade Federal de Minas Gerais, CP 702 Belo Horizonte, MG CEP 30123-970, Brazil

[◆]National High Magnetic Field Laboratory, Tallahassee, Florida 32310, United States

[□]Instituto de Química y Bioquímica, Facultad de Ciencias, Universidad de Valparaíso, Av. Gran Bretaña, 1111 Valparaíso, Chile

Supporting Information

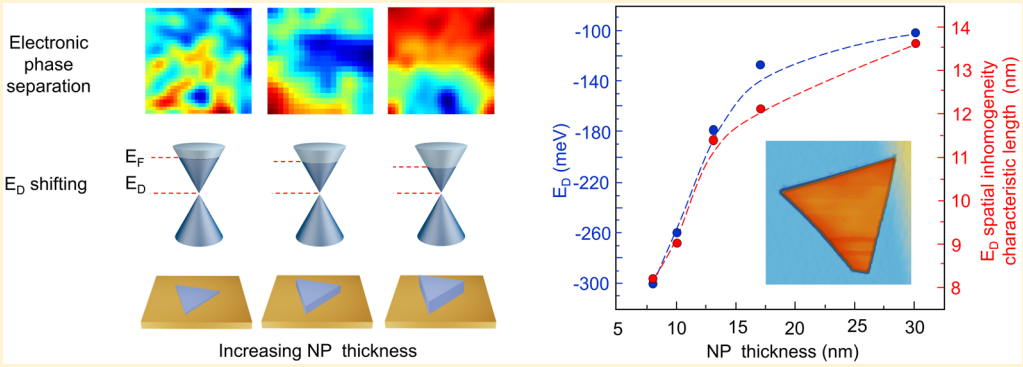

ABSTRACT: In this work we present unique signatures manifested by the local electronic properties of the topological surface state in Bi_2Te_3 nanostructures as the spatial limit is approached. We concentrate on the pure nanoscale limit (nanoplatelets) with spatial electronic resolution down to 1 nm. The highlights include strong dependencies on nanoplatelet size: (1) observation of a phase separation of Dirac electrons whose length scale decreases as the spatial limit is approached, and (2) the evolution from heavily n-type to lightly n-type surface doping as nanoplatelet thickness increases. Our results show a new approach to tune the Dirac point together with reduction of electronic disorder in topological insulator (TI) nanostructured systems. We expect our work will provide a new route for application of these nanostructured Dirac systems in electronic devices.

KEYWORDS: *Topological insulator nanostructures, Bi_2Te_3, Dirac electrons, scanning tunneling spectroscopy, phase separation, doping*

Recently both theoretical predictions and experimental measurements have demonstrated that Bi_2Te_3, a layered binary compound, is a three-dimensional (3D) topological insulator (TI), a new state of quantum matter with a bulk gap and massless Dirac surface states topologically protected with helical spin texture.[1]

The Fermi level in 3D TIs does not necessarily coincide with the Dirac point. In some of these materials, the Fermi level falls

Received: August 19, 2016
Revised: December 27, 2016
Published: December 27, 2016

DOI: 10.1021/acs.nanolett.6b03506
Nano Lett. 2017, 17, 97−103

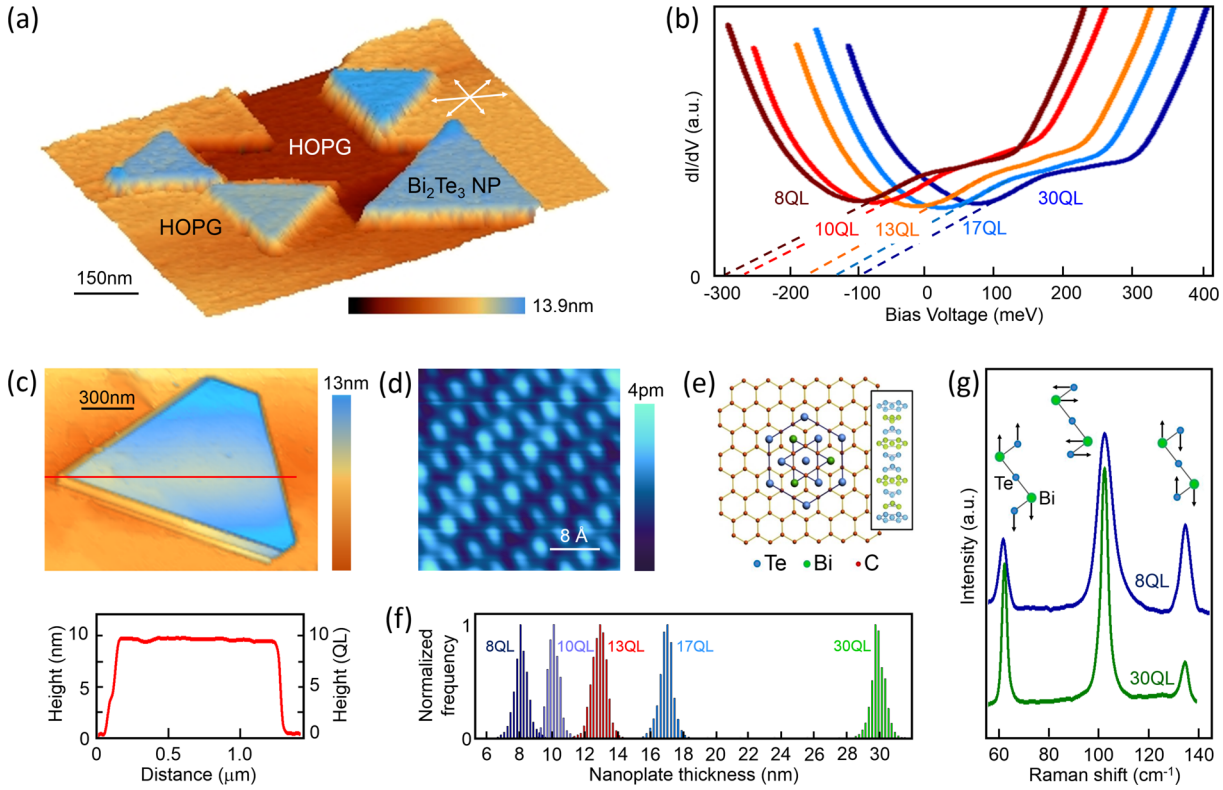

Figure 1. Structure and morphology of Bi_2Te_3 nanoplatelets. (a) STM image of a group of Bi_2Te_3 NPs grown on HOPG, V_S = 0.5 V, I = 1.0 pA. Nanoplatelets (in blue) with uniform thicknesses were aligned in the same orientation on the graphite layer (white arrows), an unequivocal sign of epitaxial growth. (b) Representative specs for Bi_2Te_3 NPs of five different thicknesses where a shift in Dirac energy was observed with respect to Fermi level. (c) Constant-current STM image of a triangular Bi_2Te_3 nanoplatelet grown on HOPG; V_S = 1 V, I = 1.0 pA, where V_S is the sample bias voltage with respect to the sample and I is the tunneling current (lower panel). Line profile along the red linecut shows that NP is 10 QL (~10 nm) in height and has a base length of 1.4 μm. (d) Atomically resolved STM image of Bi_2Te_3 nanoplatelet showing a lattice constant of 4.3 ± 0.3 Å. (e) Diagram showing final configuration for van der Waals epitaxial growth mode of Bi_2Te_3 on HOPG. Graphite exhibits a honeycomb lattice structure with C−C bond length of ~1.42 Å and Bi_2Te_3 with rhombohedral structure and a lattice constant of 4.38 Å. Lattice mismatch between substrate and Bi_2Te_3 is ~2.7%. (f) Height histogram for NPs used in the current study. (g) Raman spectra from as-grown 8 QL and 30 QL Bi_2Te_3 nanoplatelets with corresponding active Raman modes.

in either the conduction band or the valence band, and its position can strongly vary because of naturally occurring defects. In addition, a high density of charge carriers in their bulk generally mixes together bulk and surface transport characteristics. In order to separately access the remarkable properties of the surface carriers in TIs, it is vital to controllably suppress the bulk conductivity by constraining the Fermi level to the bulk bandgap.[2]

This limitation has triggered an intense search for clean TIs with the Fermi level occurring within the gap. One approach is controlling bulk carrier concentration by using an effective compensation dopant like Sn,[3,4] Cd,[4,5] Ca,[6−8] Pb,[9] Na,[10] or Sb.[11,12] However, a high dopant concentration can also introduce undesirable impurity scattering. The Fermi level in TIs can also be manipulated via gating,[13−15] structural deformation,[15,16] use of different substrates,[17] and control of thin film thickness.[18,19]

Low-dimensional TI materials, such as nanoribbons and nanoplatelets (NPs), have arisen as an excellent alternative in order to overcome the impurity scattering effect, favoring the manifestation and access to the surface states in transport measurements due to their very large surface-to-bulk ratios,[20,21] which reduce bulk carrier contribution in TI electron transport. These unique nanostructures also stand out as excellent candidates for making functional devices easy to manipulate and manufacture, creating an opportunity for versatile band structure engineering of the surface states.

To date, angle-resolved photoemission spectroscopy (ARPES) has been the predominantly used technique to determine TI band structure, employed mainly on TI thin films grown by MBE[18,22,23] and single-crystal samples cleaved in UHV conditions.[4−7] Some of these ARPES measurements, together with theoretical calculations, have revealed unconventional size effects like the evolution from 2D TI to 3D TI phase depending on film thicknesses in Bi_2Te_3[23] and Bi_2Se_3.[18] In contrast, STM and STS reports in TI crystals and MBE thin films[4,5,24,25] accessing local phenomena are less numerous than its momentum-resolved counterpart. Additionally, these studies have mainly focused on demonstrating the suppression of surface backscattering and the robust nature of MBE-grown TI systems.

Given the lack of STS measurements on TI nanostructures, we present in this work the first combined scanning tunneling microscopy (STM) and spectroscopy (STS) studies on high-quality epitaxial Bi_2Te_3 nanoplatelets grown by vapor−solid process. Here we concentrate uniquely on the nanoscale spatial limit of topological insulators (nanoplatelets), where all dimensions are well below 1 μm, in contrast to existing work in TI nanoplates.[20,21] We show that it is possible to tune the electronic properties of such high-quality TI nanomaterials

DOI: 10.1021/acs.nanolett.6b03506
Nano Lett. 2017, 17, 97−103

through its thickness, decreasing n-type charge carriers and local spatial electronic disorder as a function of thickness.

Bi_2Te_3 NPs were fabricated by a catalyst-free vapor transport and deposition process in a 12 in. horizontal tube furnace (Lindberg/Blue M) on HOPG substrate. The growth method is discussed in a previous work[20] (see Supporting Information, Figure S1 for details).

Although surface states of TIs are inherently robust against almost any surface modifications, these materials are prone to various surface chemical reactions, which are taken into account when preparing samples for devices and STM study. Particularly, continuous surface oxide growth has been observed in Bi_2Te_3[26] and Bi_2Se_3[27] after long exposure to oxygen-containing atmosphere, which causes a surface state degradation process after TI material interaction with the ambient environment. In our experiments the samples were transferred from the furnace to our STM chamber after exposure to air for just a few minutes. In order to remove the oxygen-containing layer adsorbed during transportation process (but do not change NP morphology), a few cycles of short sputtering at 200 eV were used followed by annealing at 130 C.

The final product is characterized by low temperature scanning tunneling microscopy and spectroscopy (Omicron LT-STM/STS). All topography scans were acquired in constant-current mode at 78 K in an ultrahigh vacuum chamber (pressure $<10^{-10}$ Torr) with a sample bias between 0.3 and 1 V and tunneling currents between 1 and 20 pA.

STM topography images show NPs that usually exhibit triangular and hexagonal morphologies with lateral dimensions extending up to several micrometers. A group of triangular nanoplatelets is shown in Figure 1a with color-scale representing the topographic height. Blue regions highlight NPs, whereas earth tones correspond to HOPG. In general, NPs have different thicknesses, which enable us to investigate the thickness-dependent band structure of Bi_2Te_3 NPs. Figure 1b shows a group of representative dI/dV spectra taken at the surface of NPs with different thicknesses.

We resolve the atomic lattice of a Bi_2Te_3 NP surface (Figure 1c) with a lattice constant of 4.3 ± 0.3 Å (Figure 1d). A linecut taken across these NPs shows uniform thickness and flat surface in the majority of the platelet. NP height is 10 quintuple layers (QL) as determined by the height histogram. Determined NP height is always consistent with the Bi_2Te_3 quintuple layer thickness. This correspondence suggests a quintuple layer-by-layer growth process for Bi_2Te_3 nanoplatelets.

Additionally, evidence of van der Waals epitaxial growth was found (Figure 1a) in areas where terrace edges in the substrate aligned with NP edges (NP aligned in the same orientation on the substrate). Even though, for this highly lattice-mismatched system (2.7% compressive strain, Figure 1e) the present van der Waals interface drastically relaxes the lattice matching condition encountered in heteroepitaxial growth.[28] Growth conditions for this system are far from those used in MBE (delicate control of temperature and deposition rate), which make the observed van der Waals epitaxial growth in this system remarkable. This growth mode would indicate a high crystalline quality of as-grown NPs.

Figure 1f shows the NP thickness used for the present study. Raman spectra for the thinnest (8 QL) and the thickest (30 QL) NP are shown in Figure 1g. A_{1g}^1 mode (out-of-plane mode at ~60 cm^{-1}) and E_g^2 mode (in-plane mode at ~102 cm^{-1}) are broader in the thinnest NP, which could be attributed to a previously reported disorder-induced inhomogeneous broadening and a stronger electron−phonon interaction with a concomitant reduction of phonon lifetime in TI nanostructures, which increases for thinner nanostructures.[29−31] Position of E_g^2 vibrational mode does not show a significant change, which suggests that the frequency of in-plane vibrations is not very sensitive to changes in thickness, in contrast to A_{1g}^1 and A_{1g}^2 (~132 cm^{-1}) out-of-plane vibrational modes, which shift when reducing NP thickness.

The spatial dependence of dI/dV spectra through a 50 nm linecut taken at 13 QL Bi_2Te_3 NP surface is shown in Figure 2a,

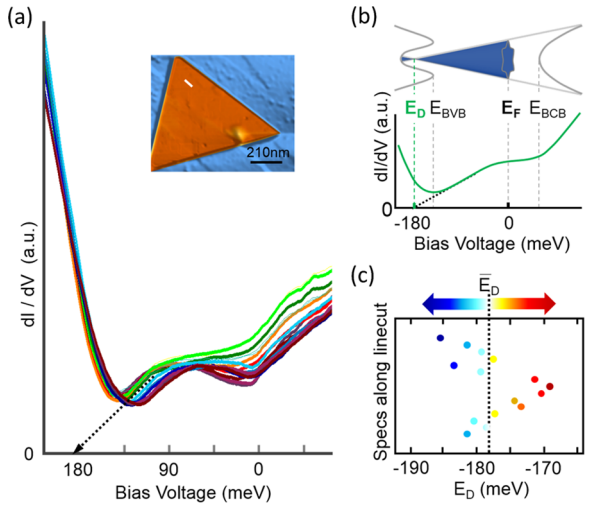

Figure 2. Spatial variation snapshots of the local density of states of Bi_2Te_3 nanoplatelets. (a) Measurements of dI/dV along a line of length 50 nm for a 13 QL. The zero-conductance point (intersection of black dashed line with 0 DOS) corresponds to the Dirac point (E_D) of the wrapped topological surface state. (b) Schematic of surface band structure and dI/dV spectrum of Bi_2Te_3 showing E_D and E_F positions. The position of the Dirac point for each spectrum is displayed in (c), where the dashed line corresponds to the mean E_D value for this nanoplatelet thickness.

providing the first glimpse of the spatial inhomogeneities and behavior analyzed in the rest of the letter. The Dirac energy (E_D) of the TI surface state (SS) for each spectrum can be obtained at the intersection of the black dashed line (extension of linearly dispersing TI surface state wrapped in bulk valence band) with zero conductance line (Figure 2b). The variations of E_D along the linecut are shown in Figure 2c with values fluctuating below (in blue) and above (in red) the mean E_D value (178 mV for this NP thickness). These local spatial fluctuations have been explored before in STS studies of doped Bi_2Te_3 crystals[32,33] and MBE thin films[34] but thus far never reported in a TI nanostructured system. Here we extend these measurements to the spatial limit.

The E_D variations for different NP thickness are quantified by the histograms seen in Figure 3a. A Gaussian has been fitted to each histogram to quantify the mean E_D value. The measured mean E_D values for different NP thickness are −301 mV for 8 QL, −260 mV for 10 QL, −178 mV for 13 QL, −127 mV for 17 QL, and −101 mV for 30 QL, indicating that E_D shifts to less negative energies when nanoplatelet thickness increases (Figure 3b). Variations of the E_D value reach a minimum for the thickest NPs, where there is a 1.5% variation around the mean E_D value (see Figure S2 for details). This variation increases for thinner nanoplatelets reaching a 14% for 10 QL and 7.3% for 8 QL.

DOI: 10.1021/acs.nanolett.6b03506
Nano Lett. 2017, 17, 97−103

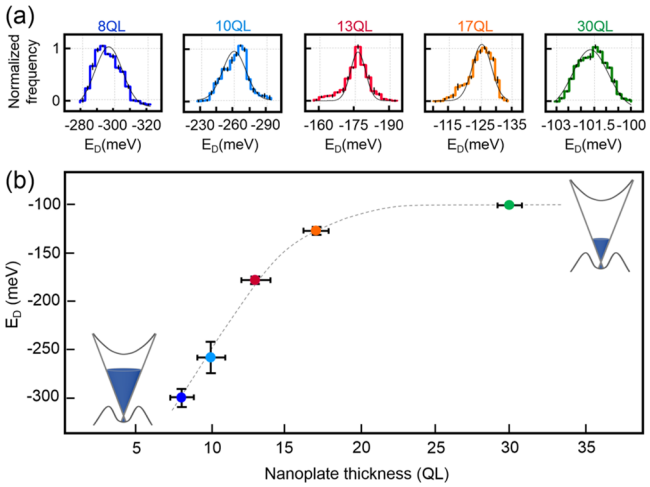

Figure 3. Bi_2Te_3 nanoplatelet thickness dependence of E_D position. (a) Histogram of E_D obtained from STS results on 8, 10, 13, 17, and 30 QL Bi_2Te_3 NPs at 78 K. A Gaussian has been fitted to each histogram to quantify fluctuations around the mean E_D value coming from STS spectra shifting. Slope variations of STS spectra are included as error bars in histograms. (b) E_D as a function of Bi_2Te_3 nanoplatelet thickness obtained from histogram in (a) with corresponding error bar. As nanoplatelet thickness increases E_D shifts to less negative energies.

As revealed by these STS measurements there is a clear thickness dependence of E_D position, showing an evolution from a heavily doped n-type to lightly doped n-type behavior. The as-grown Bi_2Te_3 compound has been reported to be either n- or p-type, depending on whether Te−Bi antisites or Te vacancies take the main role.[22,35,36] Both antisite defects (Te on Bi lattice and Bi on Te lattice) are energetically more favorable than possible vacancies in this material. However, only Bi-poor conditions (Te_{Bi}) lead to n-type transport properties.[37] The observed evolution of charge carrier doping in this nanostructured system might be a consequence of the reduction of Te_{Bi} antisite defects with Bi_2Te_3 NP thickness increase.

To visualize spatial variations we map the E_D values as a function of sample thickness with spatial resolution down to 1 nm (Figure 4). The color scale represents variation (inhomogeneity) in Dirac point with respect to Fermi level, ranging from −322 to −100 mV in real space (as seen in the color scale bar below each map). Percentage variation maps with respect to the mean E_D value are shown in Figure S2. From our local spectroscopic measurements no insulating signatures (coming from the insulating bulk state) for any NP thickness were observed.

To quantify the characteristic length scales of the E_D spatial inhomogeneity for each NP thickness, the average spatial correlation function $\langle G(\vec{r})\rangle$, and the angle-dependent spatial correlation function $\langle G_\theta(\vec{r})\rangle$ were computed for each E_D map (see Figures S3 and S4, respectively). The spatial autocorrelation function $G(\vec{r})$ of an image (STM image or STS map in our case) is defined as the statistical correlation of any two points separated by a vector $\vec{r} = \vec{r}_i - \vec{r}_j$ where $\vec{r}_i$ and $\vec{r}_j$ are the positions of those two points in the image.[38,39]

$$G(\vec{r}) = \frac{1}{N(\vec{r})} \sum_{i,j} \frac{(I_i - \langle I\rangle_1)(I_j - \langle I\rangle_2)}{\sigma_1\sigma_2}$$

where

$$N(\vec{r}) = \sum_{i,j} \delta_{\vec{r},(\vec{R}_i - \vec{R}_j)}$$

indicates the number of points at distance $\vec{r} = \vec{R}_i - \vec{R}_j$.

The average intensities (height value in an STM image or Dirac point value in an STS map) are calculated according to the expressions:

$$\langle I\rangle_1 = \sum_{i,j} \delta_{\vec{r},(\vec{R}_i - \vec{R}_j)} I_i$$

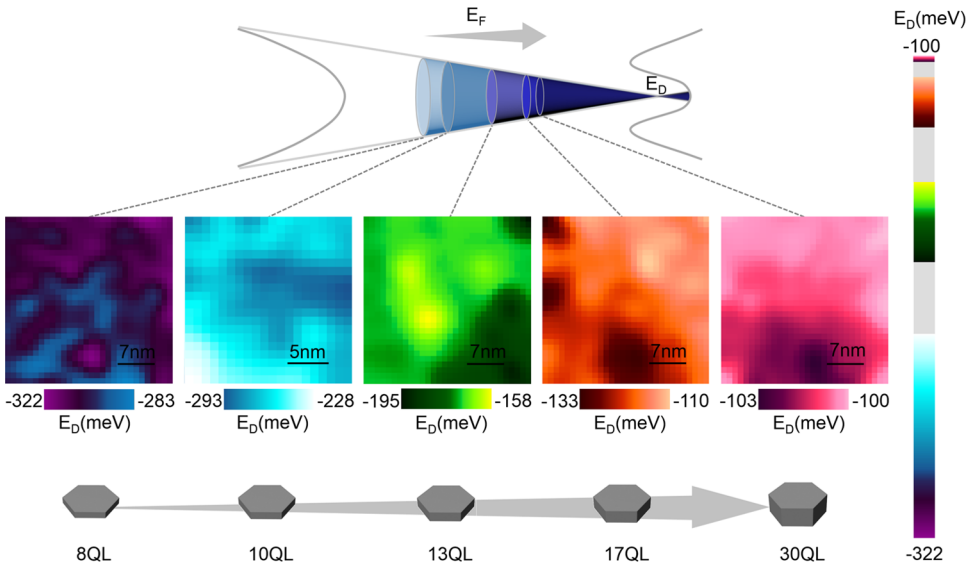

Figure 4. Spatial dependence of E_D as a function of Bi_2Te_3 nanoplatelet thickness. Map of spatial variations of the Dirac point, deduced from STS experiments for different Bi_2Te_3 NP thicknesses. Maps for 8 QL, 13 QL, 17 QL, and 30 QL are 30 × 30 nm^2, whereas for 10 QL is 20 × 20 nm^2. E_D variations range from −322 to −100 mV, with E_D overall values approaching E_F as NP thickness increases. Corresponding E_D values are represented by the color scale bar below each map. The right color scale bar shows the entire E_D range.

DOI: 10.1021/acs.nanolett.6b03506
Nano Lett. 2017, 17, 97−103

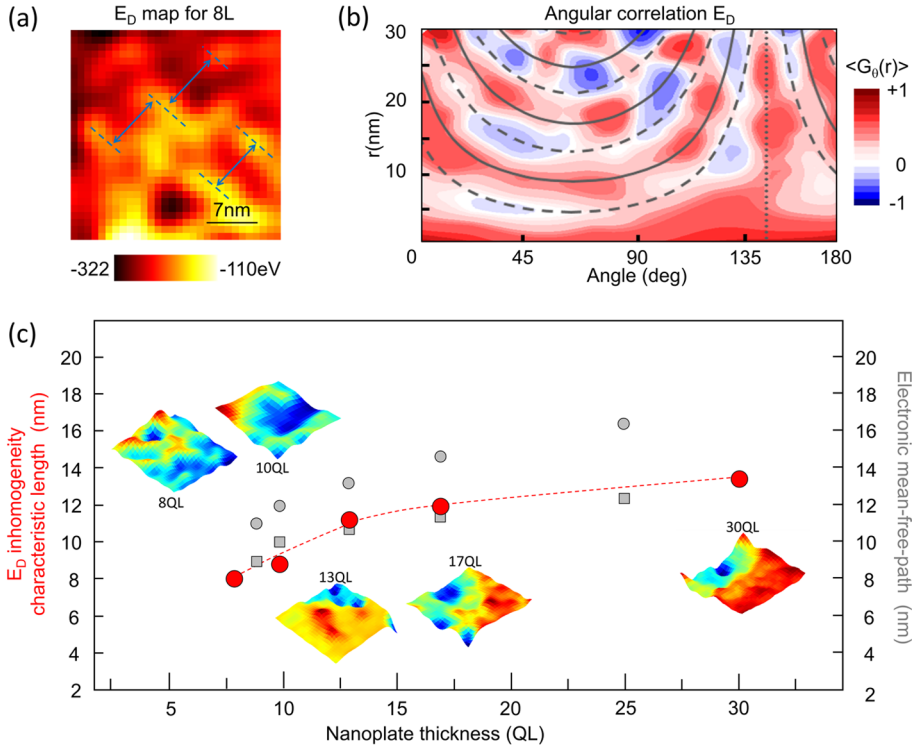

Figure 5. Thickness dependence of E_D inhomogeneity characteristic length. (a) Real space 8 QL E_D map with guidelines (in blue) to highlight the observed repeating structure. (b) Angle-dependent correlation $\langle G_\theta(\vec{r})\rangle$ analysis for 8 QL E_D map clearly shows an arc pattern, which is consistent with the real space phase separation in E_D map (See Figure S4 for other thicknesses). (c) Characteristic length scale of observed E_D spatial inhomogeneity was obtained from angular correlation analysis of STS E_D maps. E_D maps for each thickness are included as 3D images. Bulk valence (gray squares) and conduction band (gray circles) mean free path versus thickness for fully diffuse surface scattering from ref 40 are also shown for comparison purposes.

$$\langle I\rangle_2 = \sum_{i,j} \delta_{\vec{r},(\vec{R}_i-\vec{R}_j)} I_j$$

And the standard deviations are calculated according to

$$\sigma_1{}^2 = \left(\frac{1}{N(\vec{r})}\sum_{i,j} \delta_{\vec{r},(\vec{R}_i-\vec{R}_j)} I_i{}^2\right) - (\langle I\rangle_1)^2$$

$$\sigma_2{}^2 = \left(\frac{1}{N(\vec{r})}\sum_{i,j} \delta_{\vec{r},(\vec{R}_i-\vec{R}_j)} I_j{}^2\right) - (\langle I\rangle_2)^2$$

The average spatial autocorrelation function $\langle G(\vec{r})\rangle$ is the result of averaging the correlation function of all vectors with the same magnitude $|\vec{r}|$. The angle-dependent autocorrelation function $\langle G_\theta(\vec{r})\rangle$ is the result of averaging the correlation function of all vectors with orientation θ with respect to the horizontal axis and magnitude $|\vec{r}|$.

Both $\langle G(\vec{r})\rangle$ and $\langle G_\theta(\vec{r})\rangle$ of all the E_D maps reveal that there is a particular spatial pattern (with local minima and maxima), implying the presence of characteristic length scales for the observed spatial E_D inhomogeneity. The arcs in such pattern are imperfect, but repeat with a fixed periodicity, as clearly seen for the 8 QL map (Figure 5a,b), implying a pattern of phase separation of low and high carrier density domains over large length scales. The functional form of those arcs, for a system with partially disordered regions separated by a distance d and running along an angle α with respect to the horizontal, measured at an angle θ, is given by $Nd/\cos((\alpha - 90°) - \theta)$[41] (see Figure S4 for details). For real space 8 QL E_D map (Figure 5a), guidelines (in blue) highlight the observed repeating structure, which is consistent with results from angle-dependent correlation $\langle G_\theta(\vec{r})\rangle$ analysis.

In addition, close to zero cross-correlation values between E_D maps and topographies for all NP thicknesses suggest that electronic order is disconnected from local structural disorder (Figure S3). These results provide evidence that the observed phase separation of the Dirac electrons in Bi_2Te_3 NPs, which occurs in the form of stripe-like structures at repeat length d, may be self-organized. In contrast to electron−hole puddles in graphene[42] the E_D inhomogeneities observed here are actually spatially correlated with each other and to the nanoscale dimensions of the host material.

To further illustrate this point, the characteristic length scale d of such E_D spatial inhomogeneities obtained from $\langle G_\theta(\vec{r})\rangle$ analysis as a function of NP thickness is shown in Figure 5c. d values (red circles) increase with thickness, ranging from 8.2 to 13.5 nm. Electronic mean free path for bulk Bi_2Te_3 are included for reference purposes. The observed length scale increase can be interpreted as a reduction of spatial electronic disorder for thicker nanoplatelets (probably connected to the decrease of Te_{Bi} antisite defects), which is in agreement with the observed broadening of Raman spectra for thinner nanostructures. Such decreases in spatial electronic disorder with thickness suggests that electron-disorder scattering gets stronger for thinner nanoplatelets. This is in agreement with the observed evolution of the system toward lightly n-type doping, which has been reported to be related to reduction in the electron−phonon interaction and electron-disorder scattering.[37]

DOI: 10.1021/acs.nanolett.6b03506
Nano Lett. 2017, 17, 97−103

In the same way, mobility has been reported to be increased linearly with TI thin film thickness and to be saturated as the samples got thicker,[43] following the same trend as the observed spatial electronic disorder behavior. In general, an increase in mobility is due to weak strain from the substrate and reduced defect density,[43] like the one displayed in this nanostructured system.

In conclusion we found in Bi_2Te_3 nanoplatelets a clear thickness dependence of their topological surface state electronic properties. This leads to (1) the evolution from heavily n-type to lightly n-type surface doping as NP thickness increases, probably connected to a decrease in Te_{Bi} antisite defects, which leads to higher quality thicker samples and (2) increase of length scale of phase separation of Dirac electrons with NP thickness, suggesting (together with Raman results) a reduction of electron-disorder scattering and electron−phonon interaction. Under these conditions an increase in mobility is expected.

Our results show a new approach for controlling the surface doping in TI nanostructured systems, which varies in thickness together with nanoscale phase separation of the surface state electronic structure. Recently, TI nanostructures have become a promising platform to explore both fundamental questions and applications related to low dimensionality of electronic systems. According to our results, the increase of n-type charge carrier density and electronic disorder as nanostructures get thinner (and approach the spatial limit) suggests that a good approach to tune Fermi level in these TI system is the use of moderate thickness samples. We expect our work will provide a new route for application of these nanostructured Dirac systems in electronic devices.

■ ASSOCIATED CONTENT

Supporting Information

The Supporting Information is available free of charge on the ACS Publications website at DOI: 10.1021/acs.nanolett.6b03506.

(i) Detailed description of Bi_2Te_3 nanoplatelets growth method and resulting samples. (ii) E_D maps showing percentage variations with respect to mean E_D value. (iii) Autocorrelation and cross-correlation of topographies and E_D maps for all NP thickness. (iv) Angular correlation of E_D maps for all NP thickness (PDF)

■ AUTHOR INFORMATION

Corresponding Author

*E-mail: carolina.parra@usm.cl.

ORCID

Carolina Parra: 0000-0003-3819-7614

Rodrigo Segura: 0000-0003-0928-0021

Author Contributions

The manuscript was written through contributions of all authors. All authors have given approval to the final version of the manuscript.

Notes

The authors declare no competing financial interest.

■ ACKNOWLEDGMENTS

We acknowledge financial support from CONICYT inserción a la academia 791220009, Becas Santander para Jóvenes Investigadores, INCT Nanocarbono, which funded sample growth, STM/STS studies and analysis at Laboratório Nanoscopia UFMG (to C.P., T.H.R.C., F.M.S., P.H.R.G., D.D.D.R., and R.M.P.), and from the US Department of Energy, Office of Basic Energy Sciences, Division of Materials Sciences and Engineering, under contract DE-AC02-76SF00515 and Becas Chile/Programa Bicentenario de Ciencia y Tecnologia, which funded project inception and sample growth, STM/STS studies, and analysis at Stanford University/SIMES laboratories (to C.P., A.W.C., D.K., F.N., Y.C., and H.C.M.). D.K. acknowledges support from the Fundamental Research Funds for the Central Universities.

■ REFERENCES

(1) Luo, C. W.; Wang, H. J.; Ku, S. A.; Chen, H.-J.; Yeh, T. T.; Lin, J.-Y.; Wu, K. H.; Juang, J. Y.; Young, B. L.; Kobayashi, T.; Cheng, C.-M.; Chen, C.-H.; Tsuei, K.-D.; Sankar, R.; Chou, F. C.; Kokh, K. A.; Tereshchenko, O. E.; Chulkov, E. V.; Andreev, Yu. M.; Gu, G. D. *Nano Lett.* **2013**, *13* (12), 5797−5802.

(2) Kong, D.; Cui, Y. *Nat. Chem.* **2011**, *3* (11), 845−849.

(3) Chen, Y. L.; Analytis, J. G.; Chu, J.-H.; Liu, Z. K.; Mo, S.-K.; Qi, X.-L.; Zhang, H. J.; Lu, D. H.; Dai, X.; Fang, Z.; et al. *Science* **2009**, *325* (5937), 178−181.

(4) Alpichshev, Z.; Analytis, J. G.; Chu, J. H.; Fisher, I. R.; Chen, Y. L.; Shen, Z. X.; Fang, A.; Kapitulnik, A. *Phys. Rev. Lett.* **2010**, *104* (1), 016401.

(5) Alpichshev, Z.; Analytis, J. G.; Chu, J. H.; Fisher, I. R.; Kapitulnik, A. *Phys. Rev. B: Condens. Matter Mater. Phys.* **2011**, *84* (4), 041104.

(6) Hsieh, D.; Xia, Y.; Qian, D.; Wray, L.; Dil, J. H.; Meier, F.; Osterwalder, J.; Patthey, L.; Checkelsky, J. G.; Ong, N. P.; Fedorov, A. V.; Lin, H.; Bansil, A.; Grauer, D.; Hor, Y. S.; Cava, R. J.; Hasan, M. Z. *Nature* **2009**, *460* (7259), 1101−1105.

(7) Hor, Y. S.; Richardella, A.; Roushan, P.; Xia, Y.; Checkelsky, J. G.; Yazdani, A.; Hasan, M. Z.; Ong, N. P.; Cava, R. J. *Phys. Rev. B: Condens. Matter Mater. Phys.* **2009**, *79* (19), 195208.

(8) Wang, Z.; Wei, P.; Shi, J. *Front. Phys.* **2012**, *7* (2), 160−164.

(9) Aitani, M.; Sakamoto, Y.; Hirahara, T.; Yamada, M.; Miyazaki, H.; Matsunami, M.; Kimura, S. I.; Hasegawa, S. *Jpn. J. Appl. Phys.* **2013**, *52*, 110112.

(10) Wang, Y.; Xiu, F.; Cheng, L.; He, L.; Lang, M.; Tang, J.; Kou, X.; Yu, X.; Jiang, X.; Chen, Z.; Zou, J.; Wang, K. L. *Nano Lett.* **2012**, *12* (3), 1170−1175.

(11) Kong, D.; Chen, Y.; Cha, J. J.; Zhang, Q.; Analytis, J. G.; Lai, K.; Liu, Z.; Hong, S. S.; Koski, K. J.; Mo, S.-K.; Hussain, Z.; Fisher, I. R.; Shen, Z.-X.; Cui, Y. *Nat. Nanotechnol.* **2011**, *6* (11), 705−709.

(12) Arakane, T.; Sato, T.; Souma, S.; Kosaka, K.; Nakayama, K.; Komatsu, M.; Takahashi, T.; Ren, Z.; Segawa, K.; Ando, Y. *Nat. Commun.* **2012**, *3*, 636.

(13) Xiu, F.; He, L.; Wang, Y.; Cheng, L.; Chang, L.-T.; Lang, M.; Huang, G.; Kou, X.; Zhou, Y.; Jiang, X.; Chen, Z.; Zou, J.; Shailos, A.; Wang, K. L. *Nat. Nanotechnol.* **2011**, *6* (4), 216−221.

(14) Jauregui, L. A.; Pettes, M. T.; Rokhinson, L. P.; Shi, L.; Chen, Y. P. *Sci. Rep.* **2015**, *5*, 8452.

(15) Park, S. H.; Chae, J.; Jeong, K. S.; Kim, T. H.; Choi, H.; Cho, M. H.; Hwang, I.; Bae, M. H.; Kang, C. *Nano Lett.* **2015**, *15* (6), 3820−3826.

(16) Liu, Y.; Li, Y. Y.; Rajput, S.; Gilks, D.; Lari, L.; Galindo, P. L.; Weinert, M.; Lazarov, V. K.; Li, L. *Nat. Phys.* **2014**, *10* (March), 1−6.

(17) Liu, W.; Peng, X.; Wei, X.; Yang, H.; Stocks, G. M.; Zhong, J. *Phys. Rev. B: Condens. Matter Mater. Phys.* **2013**, *87* (20), 205315.

(18) He, K.; Zhang, Y.; Chang, C.-Z.; Song, C.-L.; Wang, L.-L.; Chen, X.; Jia, J.-F.; Fang, Z.; Dai, X.; Shan, W.-Y.; Shen, S.-Q.; Niu, Q.; Qi, X.-L.; Zhang, S.-C.; Ma, X.-C.; Xue, Q.-K. *Nat. Phys.* **2010**, *6*, 584.

(19) Song, C. L.; Wang, Y. L.; Jiang, Y. P.; Zhang, Y.; Chang, C. Z.; Wang, L.; He, K.; Chen, X.; Jia, J. F.; Wang, Y.; Fang, Z.; Dai, X.; Xie, X. C.; Qi, X. L.; Zhang, S. C.; Xue, Q. K.; Ma, X. *Appl. Phys. Lett.* **2010**, *97* (14), 143118.

(20) Kong, D.; Dang, W.; Cha, J. J.; Li, H.; Meister, S.; Peng, H.; Liu, Z.; Cui, Y. *Nano Lett.* **2010**, *10* (6), 2245−2250.

DOI: 10.1021/acs.nanolett.6b03506
Nano Lett. 2017, 17, 97−103

(21) Kong, D.; Randel, J. C.; Peng, H.; Cha, J. J.; Meister, S.; Lai, K.; Chen, Y.; Shen, Z. X.; Manoharan, H. C.; Cui, Y. *Nano Lett.* **2010**, *10* (1), 329−333.
(22) Wang, G.; Zhu, X. G.; Sun, Y. Y.; Li, Y. Y.; Zhang, T.; Wen, J.; Chen, X.; He, K.; Wang, L. L.; Ma, X. C.; Jia, J. F.; Zhang, S. B.; Xue, Q. K. *Adv. Mater.* **2011**, *23* (26), 2929−2932.
(23) Li, Y.-Y.; Wang, G.; Zhu, X.-G.; Liu, M.-H.; Ye, C.; Chen, X.; Wang, Y.-Y.; He, K.; Wang, L.-L.; Ma, X.-C.; Zhang, H.-J.; Dai, X.; Fang, Z.; Xie, X.-C.; Liu, Y.; Qi, X.-L.; Jia, J.-F.; Zhang, S.-C.; Xue, Q.-K. *Adv. Mater.* **2010**, *22* (36), 4002−4007.
(24) Roushan, P.; Seo, J.; Parker, C. V.; Hor, Y. S.; Hsieh, D.; Qian, D.; Richardella, A.; Hasan, M. Z.; Cava, R. J.; Yazdani, A. *Nature* **2009**, *460* (7259), 1106−1109.
(25) Zhang, T.; Cheng, P.; Chen, X.; Jia, J. F.; Ma, X.; He, K.; Wang, L.; Zhang, H.; Dai, X.; Fang, Z.; Xie, X.; Xue, Q. K. *Phys. Rev. Lett.* **2009**, *103* (26), 266803.
(26) Bando, H.; Koizumi, K.; Oikawa, Y.; Daikohara, K.; Kulbachinskii, V. A.; Ozaki, H. *J. Phys.: Condens. Matter* **2000**, *12* (26), 5607.
(27) Kong, D.; Cha, J. J.; Lai, K.; Peng, H.; Analytis, J. G.; Meister, S.; Chen, Y.; Zhang, H. J.; Fisher, I. R.; Shen, Z. X.; Cui, Y. *ACS Nano* **2011**, *5* (6), 4698−4703.
(28) Koma, A. *J. Cryst. Growth* **1999**, *201*, 236−241.
(29) Song, F.; Han, M.; Liu, M.; Chen, B.; Wan, J.; Wang, G. *Phys. Rev. Lett.* **2005**, *94* (9), 093401.
(30) Spirkoska, D.; Abstreiter, G.; Fontcuberta I Morral, A. *Nanotechnology* **2008**, *19* (43), 435704.
(31) He, R.; Wang, Z.; Qiu, R. L. J.; Delaney, C.; Beck, B.; Kidd, T. E.; Chancey, C. C.; Gao, X. P. A. *Nanotechnology* **2012**, *23* (45), 455703.
(32) Sessi, P.; Otrokov, M. M.; Bathon, T.; Vergniory, M. G.; Tsirkin, S. S.; Kokh, K. A.; Tereshchenko, O. E.; Chulkov, E. V.; Bode, M. *Phys. Rev. B: Condens. Matter Mater. Phys.* **2013**, *88* (16), 161407.
(33) Beidenkopf, H.; Roushan, P.; Seo, J.; Gorman, L.; Drozdov, I.; Hor, Y. S.; Cava, R. J.; Yazdani, A. *Nat. Phys.* **2011**, *7* (12), 939−943.
(34) Sessi, P.; Reis, F.; Bathon, T.; Kokh, K. A.; Tereshchenko, O. E.; Bode, M. *Nat. Commun.* **2014**, *5*, 5349.
(35) Hashibon, A.; Elsässer, C. *Phys. Rev. B: Condens. Matter Mater. Phys.* **2011**, *84* (14), 144117.
(36) Carva, K.; Kudrnovský, J.; Máca, F.; Drchal, V.; Turek, I.; Baláž, P.; Tkáč, V.; Holý, V.; Sechovský, V.; Honolka, J. *Phys. Rev. B: Condens. Matter Mater. Phys.* **2016**, *93* (21), 214409.
(37) Chen, C.; Xie, Z.; Feng, Y.; Yi, H.; Liang, A.; He, S.; Mou, D.; He, J.; Peng, Y.; Liu, X.; Liu, Y.; Zhao, L.; Liu, G.; Dong, X.; Zhang, J.; Yu, L.; Wang, X.; Peng, Q.; Wang, Z.; Zhang, S.; Yang, F.; Chen, C.; Xu, Z.; Zhou, X. J. *Sci. Rep.* **2013**, *3*, 2411.
(38) Fratini, M.; Poccia, N.; Ricci, A.; Campi, G.; Burghammer, M.; Aeppli, G.; Bianconi, A. *Nature* **2010**, *466*, 841.
(39) Giraldo-Gallo, P.; Zhang, Y.; Parra, C.; Manoharan, H. C.; Beasley, M. R.; Geballe, T. H.; Kramer, M. J.; Fisher, I. R. *Nat. Commun.* **2015**, *6*, 8231.
(40) Pettes, M. T.; Maassen, J.; Jo, I.; Lundstrom, M. S.; Shi, L. *Nano Lett.* **2013**, *13* (11), 5316−5322.
(41) Giraldo-Gallo, P.; Zhang, Y.; Parra, C.; Manoharan, H. C.; Beasley, M. R.; Geballe, T. H.; Kramer, M. J.; Fisher, I. R. *Nat. Commun.* **2015**, *6*, 8231.
(42) Martin, J.; Akerman, N.; Ulbricht, G.; Lohmann, T.; Smet, J. H.; Von Klitzing, K.; Yacoby, A. *Nat. Phys.* **2008**, *4*, 144.
(43) Kim, Y. S.; Brahlek, M.; Bansal, N.; Edrey, E.; Kapilevich, G. A.; Iida, K.; Tanimura, M.; Horibe, Y.; Cheong, S. W.; Oh, S. *Phys. Rev. B: Condens. Matter Mater. Phys.* **2011**, *84* (7), 073109.

DOI: 10.1021/acs.nanolett.6b03506
Nano Lett. 2017, 17, 97−103